ChemComm

COMMUNICATION

View Article Online
View Journal | View Issue

Cite this: *Chem. Commun.*, 2024, **60**, 1424

Received 30th November 2023,
Accepted 6th January 2024

DOI: 10.1039/d3cc05853k

rsc.li/chemcomm

Trifluoroethylamine-substituted solvatochromic fluorophores exhibit polarity-insensitive high brightness†

Ning Xu,[ab] Qinglong Qiao,*[a] Jie Chen,[a] Yi Tao,[a] Pengjun Bao,[a] Yinchan Zhang,[a] Jin Li[a] and Zhaochao Xu *[ab]

In this study, we have uncovered that trifluoroethylamine-substituted solvatochromic fluorophores maintain consistently high and stable fluorescence intensity in diverse polar environments, including highly polar and protic solvents. The 1,8-naphthalimide derivatives serve as a buffering fluorogenic indicator for lipid droplet morphology during the fusion process and ratiometric probe for microenvironment polarity based on Halo-tag technology.

Fluorescence-based biotechnologies hinge upon the emission properties of fluorophores.[1] Solvatochromic fluorophores undergo a wavelength shift towards longer wavelengths as local polarity increases,[2] accompanied by a notable reduction in fluorescence intensity. These distinctive traits render solvatochromic fluorophores valuable as fluorescent indicators in biological applications.[3] However, the environment-responsive variation in fluorescence intensity, while making solvatochromic fluorophores fluorogenic, presents a limitation. Their lower brightness in polar environments poses challenges for their effective utilization in identification and imaging applications within such conditions.

In recent years, substantial efforts have been dedicated to enhancing the emission performance of solvatochromic fluorophores in polar environments. When these fluorophores are excited by light, intramolecular charge transfer occurs, leading to alterations in their molecular configuration and prompting local microenvironment changes, a phenomenon known as solvent relaxation. This, in turn, imparts sensitivity to the wavelength and emission intensity of these fluorophores (see Scheme 1a). Minimizing intramolecular group twisting in the excited state and increasing solubility have proven effective strategies for improving the emission performance of fluorophores in polar settings. However, these methods still face limitations when it comes to elevating the fluorescence brightness of solvatochromic fluorophores in highly polar environments, particularly those rich in protic solvents. This challenge stems from factors like hydrogen bonding[4] and resonance energy transfer between fluorescent molecules and the solvents.[5] Ahn *et al.* introduced aliphatic chain groups into the fluorophores, creating a less polar environment in close proximity to the fluorophore.[6] Yamaguchi *et al.* observed that fluorophores employing benzophosphole oxide as the electron-withdrawing group exhibited high quantum yields in highly polar and protic solvents.[7] These findings underscore the instructive role of varying electron-withdrawing and electron-donating groups. As of now, achieving a consistently high level of brightness for solvatochromic

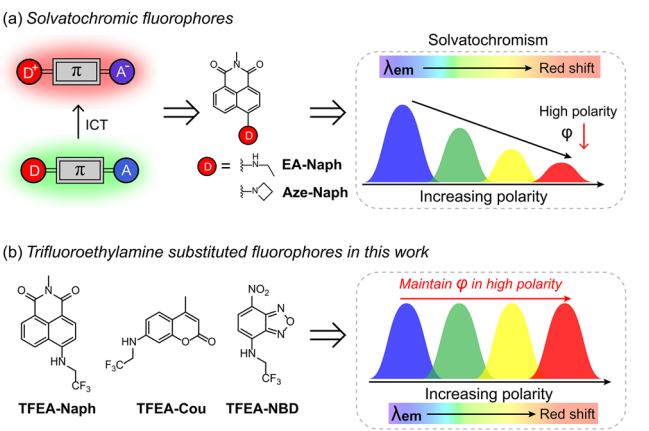

Scheme 1 (a) Traditional charge-transfer fluorophores exhibit a red shift in fluorescence emission with increasing solvent polarity accompanied by reduced emission intensity. (b) Trifluoroethylamine-substituted fluorophores in this work retain solvatochromic emission wavelength shifts with polarity changes, while enabling maintaining the stability of fluorescence intensity.

[a] *CAS Key Laboratory of Separation Science for Analytical Chemistry, Dalian Institute of Chemical Physics, Chinese Academy of Sciences, 457 Zhongshan Road, Dalian 116023, China. E-mail: qqlqiao@dicp.ac.cn, zcxu@dicp.ac.cn*

[b] *School of Chemistry Dalian University of Technology, 2 Linggong Road, Dalian 116024, China*

† Electronic supplementary information (ESI) available. See DOI: https://doi.org/10.1039/d3cc05853k

fluorophores across various polar environments has proven to be a formidable challenge.

Here, we introduced trifluoroethylamine as an electron-donating group into solvatochromic fluorophores (Scheme 1b). This modification not only retained the solvatochromism of fluorophores but also yielded a significant outcome: compared with traditional fluorophores, these modified fluorophores exhibited significantly increased brightness across solvents with varying polarities, maintaining their brightness levels effectively unchanged. Moreover, the versatility of this approach was confirmed by its successful application to different fluorophores, including 1,8-naphthalimide, coumarin, and NBD. These solvatochromic fluorophores, which maintain a consistent fluorescence intensity, can find unique applications in the fields of cellular sensing and imaging.

We initiated our investigation by measuring the UV-vis absorption and fluorescence spectra of **TFEA-Naph** in various solvents (Fig. S1, ESI† and Fig. 1a). A red-shift in emission wavelengths was observed as solvent polarity increased, indicating that trifluoroethylamine did not affect the solvatochromism of the fluorophore. We then conducted a comparative analysis of the quantum yield of **TFEA-Naph** in nonpolar, polar aprotic, and polar protic solvents to investigate its polarity-dependent fluorescence intensities. In comparison to the conventional ethylamine-substituted naphthalimide without fluorine atom modification (**EA-Naph**), **TFEA-Naph** exhibited a significant increase in quantum yield across all solvents (Fig. 1b). Fluorescence quantum yields of **TFEA-Naph** in organic solvents are between 0.8–0.9 (Table S1, ESI†). Notably, unlike **EA-Naph**, which maintained high quantum yields in nonpolar and polar aprotic solvents but exhibited a significant decrease in polar protic solvents (Fig. S2a, ESI†), **TFEA-Naph** consistently maintained relatively stable quantum yields across nonpolar and polar solvents. While the quantum yield of **TFEA-Naph** in water did decrease, it remained above 0.5. Additionally, **Aze-Naph**, which experienced enhanced quantum yields by inhibiting twisted intramolecular charge transfer (TICT),[4a,8] exhibited solvent-dependent fluorescence intensity changes following a similar pattern as **EA-Naph** (Fig. S2b, ESI†). This suggests that TICT inhibition does not resolve the issue of low fluorescence intensity in highly polar and protic solvents.

Continuing our investigation, we sought to determine whether this approach could be extended to other solvatochromic fluorophores, such as coumarin and NBD. As illustrated in Fig. 1c and Fig. S3 (ESI†) and detailed in Table S2 (ESI†), **TFEA-Cou** exhibited consistently high quantum yields (ranging from 0.8 to 1) across all solvents. Similarly, **TFEA-NBD** displayed favorable quantum yields (ranging from 0.3 to 0.6) in both polar and nonpolar solvents, as depicted in Fig. 1d and Fig. S3 (ESI†) and detailed in Table S3 (ESI†). When assessing the stability of fluorescence intensity for these compounds across all solvents, it became evident that trifluoroethylamine-substituted fluorophores exhibited the least dispersion in relative quantum yield, as indicated in Fig. 1e and f. These findings strongly suggest that introducing trifluoroethylamine as an electron-donating group into solvatochromic fluorophores constitutes a versatile method for enhancing brightness in polar environments while maintaining consistent fluorescence intensity across varying polarities.

The variations in brightness observed among these three dyes in water and organic solvents, such as ethanol, are indeed quite distinct. In ethanol, the quantum yield for coumarin **TFEA-Cou** is 0.9, and this value increases to 0.94 in water. On the other hand, the quantum yield of naphthalimide-based **TFEA-Naph** drops from 0.85 to 0.5 in the transition from ethanol to water. The most significant change is seen with NBD-based **TFEA-NBD**, where the quantum yield drops steeply from 0.49 in ethanol to 0.067 in water. When comparing quantum yield reductions in water with polar organic solvents, these decreases are commonly attributed to three primary factors: solubility, hydrogen bonding with water molecules, and resonance energy transfer with water molecules (Fig. S4a, ESI†). To gain insight into the underlying causes for the reduction in quantum yield in water, we conducted several experiments. We compared the quantum yield of **TFEA-Naph** in water with that in D_2O, examined the quantum yield of **TFEA-Naph** in mixed solutions of H_2O and DMSO with varying ratios, and investigated the changes in quantum yield as water solubility increased by introducing water-soluble groups into **TFEA-Naph**. As depicted in Fig. S4b (ESI†), the increase in water solubility of the dye molecules did not result in a change in quantum yield. Furthermore, the quantum yield for all dye molecules decreased significantly in D_2O (Fig. S5, S6 and Table S4–S6, ESI†). In the mixed solution, quantum yield reduction only occurred when the water content exceeded 90% (Fig. S4b for **TFEA-Naph** and Table S7 for **TFEA-NBD**, ESI†). These findings suggest that, for the **TFEA-Naph**, the decrease in quantum yield in water is likely not due to solubility or hydrogen bonding with water. Instead, it is most probably attributed to resonance energy transfer between naphthalimide and water. In the mixed solution, when the proportion of DMSO dominates, it obstructs the interaction between water and fluorescent molecules, thereby inhibiting resonance energy transfer between them. Consequently, the emission wavelengths of coumarin, naphthalimide, and NBD gradually increase, aligning more favorably in terms of energy level matching with water.[5] This leads to a progressively pronounced decrease in quantum yield in water.

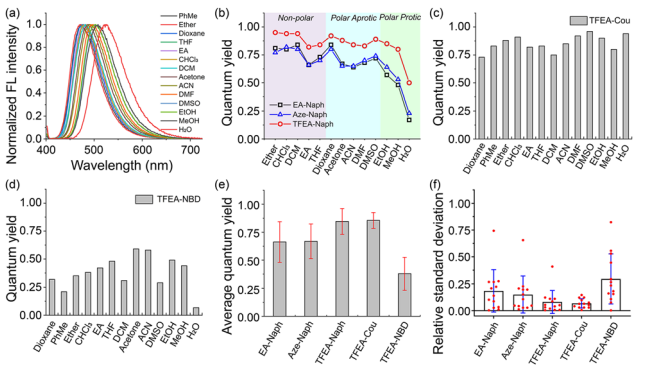

Fig. 1 (a) Normalized emission spectra of **TFEA-Naph** (5 μM, λ_{ex} = 400 nm); (b) Quantum yields of **EA-Naph**, **Aze-Naph** and **TFEA-Naph** in different solvents; Quantum yields of **TFEA-Cou** (c) and **TFEA-NBD** (d) in different solvents; Average quantum yields (e) and relative standard deviation of quantum yields (f) in different solvents for **EA-Naph**, **Aze-Naph**, **TFEA-Naph**, **TFEA-Cou** and **TFEA-NBD**.

The emerging fluorescence properties of fluorescent dyes continually present opportunities for new applications in biological research. For instance, the fluorescence blinking breaks the diffraction limit,[9] while the use of fluorogenic probes enables wash-free fluorescence imaging.[3,10] These unique solvatochromic dyes, with the capacity to maintain consistent brightness across diverse polar environments, hold great promise for pioneering biological applications. We anticipate that the target specificity inherent in solvatochromic fluorophores can be effectively merged with the imaging capabilities of high-brightness dyes. This fusion of attributes is poised to open up exciting avenues in biological research, offering innovative solutions and enhancing our ability to explore and understand the intricacies of biological systems.

Live cell imaging experiments have revealed that **TFEA-Naph** demonstrates excellent cell membrane permeability and targeting properties, setting it apart from **TFEA-Cou** and **TFEA-NBD**, which exhibit poor membrane permeability and weak fluorescence (Fig. S9, ESI†). As a result, our subsequent cell imaging experiments focused on utilizing **TFEA-Naph**. Leveraging the polarity-sensitive emission wavelength of **TFEA-Naph**, we can selectively target different cellular components. For instance, short-wavelength emissions from **TFEA-Naph** are concentrated in lipid droplets, while long-wavelength emissions originate from the cytosol (Fig. S9a, ESI†). This selective approach allows us to specifically image lipid droplets by choosing a short-wavelength imaging window.

One valuable application of solvatochromic fluorophores relies on their ability to undergo wavelength shifts for ratiometric detection. However, their intracellular use has been somewhat constrained by their lower fluorescence intensity in highly polar environments. To assess the ratiometric imaging capabilities, we synthesized **TFEA-Naph-Halo** and labeled this probe to specific proteins in different organelles through Halo-tag technology to achieve imaging of different organelles. Given that the quantum yield of **TFEA-Naph-Halo** is lower in water compared to organic solvents, **TFEA-Naph-Halo** delivers exceptional wash-free fluorescence imaging performance for cell nuclei, actin and mitochondria (Fig. 2 and Fig. S10, S11, ESI†). *In situ* spectral analysis revealed that the maximum emission wavelength within the nucleus is 490 nm (Fig. S10c and d, ESI†). As the imaging window transitions from shorter wavelengths to longer wavelengths, the signal-to-noise ratio in nuclear imaging steadily increases, escalating from 3.3 to 9.5 (Fig. 2b). We harnessed the signals collected within two imaging windows, spanning 425–475 nm and 500–600 nm, for ratio processing, enabling us to create polarity distribution images within the cell nucleus (Fig. 2c). With the same ratiometric imaging method, it's also possible to detect and visualize actin polarity (Fig. 2d and e).

In cells that were not transfected with the halo protein, TFEA-Naph-Halo exhibited a remarkable ability to selectively stain lipid droplets, owing to its heightened lipophilicity (Fig. S12, ESI†). The maximum emission wavelength of **TFEA-Naph-Halo** was observed to be approximately 455 nm within lipid droplets, affirming the low-polarity environment of

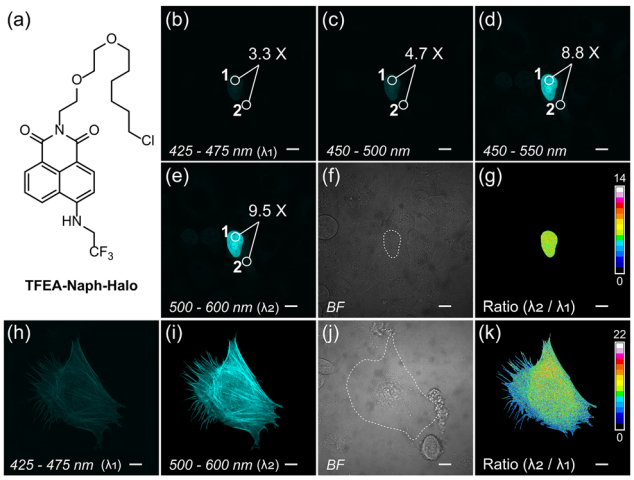

Fig. 2 (a) Chemical structure of **TFEA-Naph-Halo**; (b)–(f) Confocal imaging of nucleus transfected with Halo-H2B plasmid under different collection channels using **TFEA-Naph-Halo**; (g) Ratio fluorescence plot of TFEA-Naph-Halo by a dual-emission channel (λ_1 = 425–475 nm; λ_2 = 500–600 nm; ratio = λ_2/λ_1) at λ_{ex} = 405 nm; (h–j) Confocal imaging of actin in HeLa cells expressed Halo Tag protein under different collection channels using **TFEA-Naph-Halo**; (k) Ratio fluorescence plot of **TFEA**-Naph-Halo by a dual-emission channel (λ_1 = 425–475 nm; λ_2 = 500–600 nm; ratio = λ_2/λ_1) at λ_{ex} = 405 nm. Scale bar = 10 μm.

lipid droplets (Fig. S13 and S14, ESI†). Furthermore, through the application of ratiometric imaging, we discerned that lipid droplets situated at different locations within the cell exhibited varying degrees of polarity (Fig. S13b and c, ESI†).

The fusion of lipid droplets constitutes a crucial dynamic process for facilitating substance transport between these droplets and executing various physiological functions. We employed SIM super-resolution imaging microscopy to measure fluorescence intensity within the lipid droplets, employing position tracking techniques to unveil alterations in lipid droplet morphology throughout the fusion process.

Through a series of fluorescence recovery after photobleaching (FRAP) experiments,[11] we demonstrated that **TFEA-Naph-Halo** possesses the capacity to act as a buffering fluorogenic probe (Fig. 3a, b and Fig. S15, ESI†). This dynamic process ensures a consistent number of fluorescent molecules remain within the lipid droplets, thus achieving stable super-resolution fluorescence imaging to monitor the fusion process of lipid droplets. Imaging the fluorescence intensity within lipid droplets provides clear insights into the dynamic changes in lipid droplet morphology during the fusion process, which can be segmented into three distinct stages (Fig. 3):

Initial fusion stage: At the outset, lipid droplets maintain their spherical structures. The distribution of fluorescence intensity within the lipid droplets follows a parabolic shape. As two lipid droplets initiate fusion upon contact, their sizes remain unchanged. However, the fluorescence intensity at the fusion site gradually intensifies from weak to strong, approaching the maximum fluorescence intensity within the lipid droplet. This indicates that during the initial fusion stage, lipids move to converge from both directions towards the central

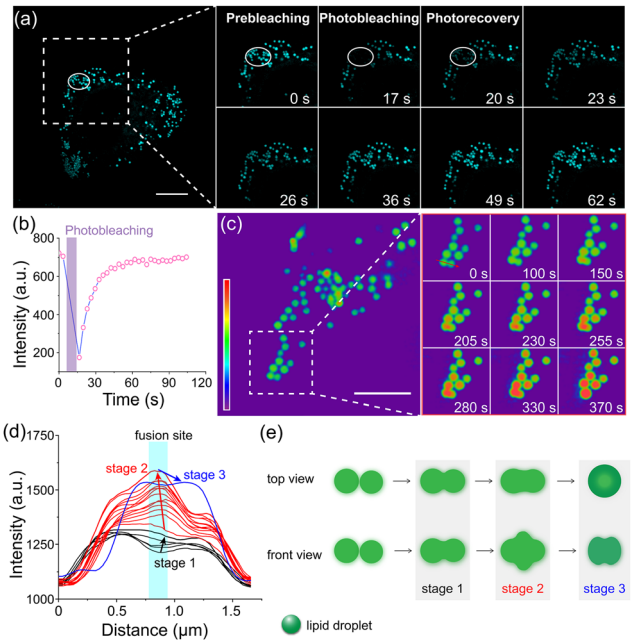

Fig. 3 (a) Confocal images of **TFEA-Naph-Halo** during photobleaching and photorecovery processes. White circles highlighted the bleaching area. Scale bar = 10 μm; (b) Relative intensity of the bleaching area in (a) during photobleaching and photorecovery processes. (c) SIM image of living HeLa cells with **TFEA-Naph-Halo** and the locally enlarged images of the boxed region for transport process of neutral lipids. Scale bar = 5 μm; (d) Relative intensity of the red line during lipid droplets fusion process in (c); (e) The model of three stages of dynamic changes in lipid droplet morphology during the fusion process.

contact position (*X*-axis direction). The fusion then transitions into the second stage.

Intermediate fusion stage: In the second stage, the transport of lipids from both directions towards the central position intensifies. A distinctive morphology emerges at the fusion point—a depression forms along the *Y*-axis direction, accompanied by a bulge in the vertical *Z*-axis direction. When viewed from above, this fusion body resembles a dumbbell shape, while an oblong spindle shape is observed when viewed directly. This phase is marked by a reduction in the lateral size of the fusion body and slight positional oscillation, yet the fusion site remains fixed in space. In this stage, materials from both lipid droplets are transported to the center, with material movement at the fusion point slowing significantly due to collisions. This deceleration leads to oscillations in material at the far ends of the fusion body, causing positional fluctuations at both ends of the fusion body. The second stage accounts for the majority of the fusion process time (300 seconds).

Final fusion stage: The third stage commences as the depression at the fusion body's center rapidly expands outward along the *Y*-axis direction, while the central bulge recedes in the *Z*-axis direction. Simultaneously, the fusion body changes from a thin strip in the center to a round shape. In comparison to the second-stage fusion, the lateral size of this singular lipid droplet is significantly reduced. The fluorescence intensity at the center of the lipid droplet is lower than that of its surroundings. During this stage, the fused lipid droplets adopt a donut-like shape, likely due to the vigorous movement of materials within the fusion body. This movement results in outward expansion along the *X* and *Z* axes and inward contraction along the *Y* axis. Following this phase of dynamic changes, the fused lipid droplets ultimately stabilize and revert to their spherical structures.

In summary, we have developed several solvatochromic fluorophores, each featuring the introduction of trifluoroethylamine substitutions as an electron-donating group. Notably, these fluorophores have demonstrated remarkable effectiveness in maintaining solvatochromic emission wavelength shifts in response to changes in polarity, all while ensuring the stability of brightness. Furthermore, we have illustrated their excellent performance and potential applications in cellular sensing and dynamic imaging. The intricate insights we've gained into the ratiometric imaging of different organelles and lipid droplet fusion process, enabled by the spectral properties of these fluorophores, have sparked our enthusiasm to explore their utilization in imaging a wider array of dynamic cellular processes.

This work is supported by the National Natural Science Foundation of China (22278394, 22078314, 21908216) and Dalian Institute of Chemical Physics (DICPI202227, DICPI202142).

Conflicts of interest

There are no conflicts to declare.

Notes and references

1 L. D. Lavis and R. T. Raines, *ACS Chem. Biol.*, 2008, **3**, 142.
2 (*a*) Q. Qiao, W. Liu, W. Chi, J. Chen, W. Zhou, N. Xu, J. Li, X. Fang, Y. Tao, Y. Zhang, Y. Chen, L. Miao, X. Liu and Z. Xu, *Aggregate*, 2023, **4**, e258; (*b*) W. Liu, J. Chen, Q. Qiao, X. Liu and Z. Xu, *Chin. Chem. Lett.*, 2022, **33**, 4943; (*c*) Y. Zhang, W. Zhou, N. Xu, G. Wang, J. Li, K. An, W. Jiang, X. Zhou, Q. Qiao, X. Jiang and Z. Xu, *Chin. Chem. Lett.*, 2023, **34**, 107472.
3 A. S. Klymchenko, *Acc. Chem. Res.*, 2017, **50**, 366.
4 (*a*) X. Liu, Q. Qiao, W. Tian, W. Liu, J. Chen, M. J. Lang and Z. Xu, *J. Am. Chem. Soc.*, 2016, **138**, 6960; (*b*) S. F. Lee, Q. Vérolet and A. Fürstenberg, *Angew. Chem., Int. Ed.*, 2013, **52**, 8948.
5 J. Maillard, K. Klehs, C. Rumble, E. Vauthey, M. Heilemann and A. Fürstenberg, *Chem. Sci.*, 2021, **12**, 1352.
6 S. Singha, D. Kim, B. Roy, S. Sambasivan, H. Moon, A. S. Rao, J. Y. Kim, T. Joo, J. W. Park and Y. Rhee, *Chem. Sci.*, 2015, **6**, 4335.
7 E. Yamaguchi, C. Wang, A. Fukazawa, M. Taki, Y. Sato, T. Sasaki, M. Ueda, N. Sasaki, T. Higashiyama and S. Yamaguchi, *Angew. Chem., Int. Ed.*, 2015, **54**, 4539.
8 W. Liu, Q. Qiao, J. Zheng, J. Chen, W. Zhou, N. Xu, J. Li, L. Miao and Z. Xu, *Biosens. Bioelectron.*, 2021, **176**, 112886.
9 M. Lelek, M. T. Gyparaki, G. Beliu, F. Schueder, J. Griffié, S. Manley, R. Jungmann, M. Sauer, M. Lakadamyali and C. Zimmer, *Nat. Rev. Methods Primers*, 2021, **1**, 39.
10 J. Li, Q. Qiao, Y. Ruan, N. Xu, W. Zhou, G. Zhang, J. Yuan and Z. Xu, *Chin. Chem. Lett.*, 2023, **34**, 108266.
11 J. Chen, C. Wang, W. Liu, Q. Qiao, H. Qi, W. Zhou, N. Xu, J. Li, H. Piao, D. Tan, X. Liu and Z. Xu, *Angew. Chem., Int. Ed.*, 2021, **133**, 25308.